New wideband large aperture open-ended coaxial microwave probe for soil dielectric characterization

Alex Gélinas[1,2], Bilal Filali[3], Alexandre Langlois[2,4], Alex Mavrovic[1,2], François Demontoux[5], and Alexandre Roy[1,2]

[1]*Centre de recherche sur les interactions bassins versants – écosystèmes aquatiques (RIVE), Université du Québec à Trois-Rivières*
[2]*Centre d'Études Nordiques (CEN), Université Laval*
[3]*PhyVertX Technologies Inc.*
[4]*Centre d'Applications et de Recherches en Télédétetcion (CARTEL), Université de Sherbrooke*
[5]*Laboratoire de l'Intégration du Matériau au Système (IMS), Université de Bordeaux*

***Abstract*—We present a unique Open-Ended Coaxial Probe that has the capability of accurately measuring the permittivity of heterogeneous materials, such as soil, due to its large aperture. The probe was designed to work at frequencies ranging from 0.5 to $18\,\mathrm{GHz}$, which is a particularly important range for microwave remote sensing applications, and more precisely the Terrestrial Snow Mass Mission (TSMM). TSMM aims at launching a new satellite equipped with a dual Ku-band radar (13.5 and $17.2\,\mathrm{GHz}$) for snow monitoring. At Ku-band frequencies, the backscattered radar signal contains information about the snow, but can also contain a contribution from the soil. Knowing the soil permittivity will enable a better representation of this soil contribution to the radar signal to obtain more accurate snow data such as Snow Water Equivalent (SWE). To demonstrate the accuracy and repeatability of the probe, solutions of known permittivity were measured, and the results were compared to their theoretical values. Then, tests for approximating the penetration depth of the probe signal were conducted with dry and wet paper. Afterwards, a protocol to use the probe to compute the permittivity of soil samples in freeze/thaw cycles was developed. The permittivity of commercial sand and arctic organic soil from Cambridge Bay (Nunavut) are presented for different relevant microwave remote sensing frequencies selected on the full range of the probe and temperatures (-20 to $20\,^{\circ}\mathrm{C}$) according to the new protocol. The main goal of this paper is to present the probe and its potential use in the field of remote sensing, especially for active Ku-band (13 to $20\,\mathrm{GHz}$) remote sensing applications, where there is little work done.**

***Index Terms*—Coaxial probe, Microwaves, Remote Sensing, Permittivity, Soil**

I. Introduction

RECENT DEVELOPMENTS in active microwave remote sensing showed the potential of Syntethic Aperture Radar (SAR) for monitoring important snow characteristics. More precisely, studies demonstrated the high sensitivity of SAR backscattering in the Ku-band domain (12 to $18\,\mathrm{GHz}$) to Snow Water Equivalent (SWE) [1]–[3]. Following SWE temporal and spatial variation in location where the snow coverage spans more than 6 months per year is of utmost importance for hydrological cycles [4], [5], surface energy balance [6], [7], biogeochemical cycles [4], [8], among others. The significance of seasonal snowmelt and SWE in delivering freshwater is of great importance for the well-being of Canadians, supporting a diverse array of economic sectors and sustaining ecosystems. Simultaneously, it introduces risks through contributions to floods and the perpetuation of drought events. These properties and developments led to the beginning of a joint mission from Canadian Spatial Agency (CSA) and Environment and Climate Change Canada (ECCC), Terrestrial Snow Mass Mission (TSMM) [9], [10], which aims at launching a dual Ku-band SAR ($13.5\,\mathrm{GHz}$ and $17.2\,\mathrm{GHz}$) aboard a satellite for snow monitoring in the Northern Hemisphere. Moreover, Ku-band SAR mounted on a satellite would offer regular high resolution (few meters) SWE data for remote locations around the globe, under various meteorological conditions [11]. Indeed, Ku-band radar signal has low interactions with atmospheric particles such as water vapor in clouds and is completely independent of solar radiations.

However, there are still lots of challenges for SWE inversion using the Ku-band SAR backscatter signal. Indeed, the backscattering signal is not only influenced by Snow Water Equivalent, but also by other snowpack characteristics such as microstructure and liquid water content, and by the substrate under the snow (sea ice, fresh water ice, soil, etc.) and vegetation cover. To overcome these obstacles, modelization of the signal via microwave radiative transfer models such as Snow Microwave Radiative Transfer (SMRT) [12] is used to disentangle the effect from each contribution, enabling SWE retrieval from the backscattering signal. Most of the existing models for active remote sensing backscatter were built for lower microwave frequencies ($<6\,\mathrm{GHz}$, [13]), whereas SMRT was designed to work in a frequency range that encompasses the TSMM mission dual Ku-band frequencies. Moreover, SMRT was specifically conceived to include parameters such as snow microstructure and the substrate characteristics. Nonetheless, SMRT developers mention that there is a need for more precise wave diffusion models at snow/substrate interface [12]. Soil contribution is still misrepresented by the model and brings some uncertainty in the snow signal produced [2]. In order to model the soil contribution to the total backscattering signal, an important parameter to understand is the soil relative permittivity (hereafter referred to as permittivity).

Indeed, knowing the soil permittivity allows to model the soil influence over the total signal. In current radiative transfer models targeting snow characteristics, frozen soil permittivity

is often set to a constant close to that of dry soil [14], [15]. This is due to the lack of knowledge regarding the spatial and temporal variability of frozen soil permittivity. Soil permittivity greatly depends on soil water content [16] where water permittivity is relatively high ($\varepsilon' \approx 80$ at L-band) compared to dry soil ($\varepsilon' \approx 2.5$ [17]) or ice ($\varepsilon' \approx 3.2$ [18]). This means that having unfrozen water in the soil would greatly increase the permittivity, hence modifying the soil backscattering signal. Models for soil permittivity (called dielectric mixing models, [14], [19]–[21]) have already been developed in the past, but none include the frequencies targeted by TSMM for multiple temperatures.

In this context, the goal of this article is to present a novel Open-Ended Coaxial Probe (OECP) with an operating frequency range from 0.5 to 18 GHz, able to measure the permittivity of a flat material or liquid. The probe aperture (the measurement plane) is sufficiently large to integrate a representative average permittivity over non-homogeneous soil. In this study, we present the novel OECP and its precision over its full operating range as well as tests to estimate the probe signal penetration depth. Then, liquids of known permittivity are used to compare the probe's results to theoretical values in order to validate the probe calibration. Finally, a protocol was developed to measure the soil permittivity in a controlled varying temperature environment (from -20 to $20\,^{\circ}$C). Two different soil types (sand and arctic organic soil) were analyzed following the new protocol.

II. Theory and Methodology

A. Probe setup

The OECP used in this project was developed by PhyVertX Technologies Inc., it is an adaptation for higher frequencies of the probe described in [22]. The probe is made of two conducting coaxial cylinders with a Polytetrafluoroethylene (PTFE) core akin to a coaxial cable. The inner cylinder has a $2a = 4\,\text{mm}$ diameter while the outer cylinder diameter is $2b = 13.2\,\text{mm}$ (Figure 1A).

The probe's dimensions were chosen sufficiently large for the measurement of heterogeneous material such as soil while being able to cover a frequency range from 0.5 GHz up to 18 GHz. To operate the OECP, a 1-port Vector Network Analyzer (VNA), the R180 (0.001 to 18 GHz, frequency resolution of 50 Hz) from Copper Mountain® Technologies was used. All the instruments, connectors and cables in the setup have an impedance of $50\,\Omega$ to reduce unwanted reflections. In order to connect the OECP (SMA connector) to the VNA (Type-N connector), a solid adaptor was used to eliminate possible noise that could occur in cables or semi-rigid adaptors. The VNA was then connected to a computer and was operated by the RVNA software distributed by the company (Figure 1C). Once the setup assembled, two calibrations were performed to ensure the accuracy of the measurements: the first calibrates the cables and connectors connected to the probe using a specific calibration kit (system calibration) and the second calibrates the probe measurement plane, i.e. the aperture of the probe (probe calibration, see Section II-C for more details).

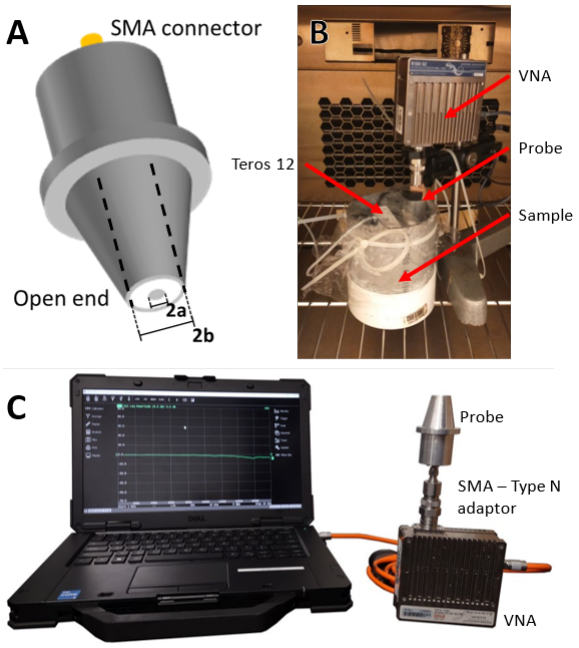

Fig. 1. **A:** OECP scheme, where the diameter of the conductive core (2a) is 4 mm and the outer diameter of the PTFE core (2b) is 13.2 mm; **B:** Experimental setup for the temperature cycle measures; **C:** VNA and OECP, connected to the computer with the operating software for the VNA

B. Probe measurement principle

In order to get the permittivity at the aperture of the probe, the VNA measures the reflection coefficient ρ. This measured reflection coefficient ρ is then linked to the real reflection coefficient Γ through the scattering parameters of the probe with the Equation 1 [23]:

$$\Gamma = \frac{\rho - S_{11}}{S_{22}\rho + S_{12}S_{21} - S_{11}S_{22}} \tag{1}$$

Where the $S_{i,j}$ $(i,j \in \{1,2\})$ are the probe scattering parameters. The probe calibration, detailed in Section II-C, is made to find those $S_{i,j}$ using liquids of known permittivity. Γ is also related to the admittance of both the probe (Y_0) and the material under test ($Y(\varepsilon)$) with Equation 2 [23]:

$$\Gamma = \frac{Y(\varepsilon) - Y_0}{Y(\varepsilon) + Y_0} \tag{2}$$

Finally, the permittivity of the medium ($varepsilon_r$) can be deduced from its admittance ($Y(K)$) by solving Equation 3 [24]:

$$Y(K) = \frac{\varepsilon_r Z_\nu}{\ln({}^{a}/_{b})} \int_0^\infty \frac{[J_0(\beta p) - J_0(\alpha p)]^2}{p\sqrt{\varepsilon_r - p^2}} dp \tag{3}$$

Where $K = {}^{2\pi f}/_{c}$ is the wave number in vacuum, $Z_\nu = \sqrt{{}^{\mu_0}/_{\varepsilon_0}} \approx 376.7303\,\Omega$ is the vacuum impedance, $\alpha = Ka$, $\beta = Kb$ are geometric parameters, J_0 is the zero$^{\text{th}}$ order Bessel function of the first kind and p is the integration variable.

C. Calibration

Both calibration principles are based on the Short Open Load (SOL) one-port method, where measurements of known

standards are compared to their theoretical values for all three calibration standards (open, short-circuit and load). The measurements are then processed in order to find the $S_{i,j}$ (Equation 1) parameters of the calibration plane. To get accurate measurements, two calibrations are necessary, the first, the system calibration, is made at the probe connection plane to calibrate the VNA and the connectors and cables connected to the probe. For this first calibration, a S2611 calibration kit from Copper Mountain® Technologies is used. The kit connectors have a $50\,\Omega$ impedance and includes all the necessary standards. Once the system is calibrated, the probe is connected at the end of the line and is also calibrated.

The probe calibration was made specifically for the probe using the SOL method at the measurement plane (the aperture). The open standard corresponds to a measure in the air, the short-circuit standard was made by covering the probe with a conducting metal such as copper and the load standard was a saline (NaCl) water solution ($35\,\mathrm{ppm}$).

Using these three standards, Equation 1 can be written for each $\rho_{1,2,3}$ and $\Gamma_{1,2,3}$, where $\Gamma_{1,2,3}$ is deduced from $Y_{1,2,3}$ using Equation 2. Solving these three equations leads to a system of three equations for three unknown variables (Equation 4):

$$\begin{aligned} S_{11} &= \frac{\Gamma_1\Gamma_2\rho_3(\rho_1-\rho_2)+\Gamma_1\Gamma_3\rho_2(\rho_3-\rho_1)+\Gamma_2\Gamma_3\rho_1(\rho_2-\rho_3)}{\Gamma_1\Gamma_2(\rho_1-\rho_2)+\Gamma_1\Gamma_3(\rho_3-\rho_1)+\Gamma_2\Gamma_3(\rho_2-\rho_3)} \\ S_{22} &= \frac{\Gamma_1(\rho_2-S_{11})+\Gamma_2(S_{11}-\rho_1)}{\Gamma_1\Gamma_2(\rho_2-\rho_1)} \\ S_{12}S_{21} &= \frac{(\rho_1-S_{11})(1-S_{22}\Gamma_1)}{\Gamma_1} \end{aligned} \tag{4}$$

After the probe calibration, two test liquids were used to assess the probe calibration quality. The first test liquid was a saline solution at $20\,\mathrm{ppm}$ and the second one was methyl hydrate. Both computed permittivity were compared to the theoretical permittivity provided by Nyshadham, Sibbald, and Stuchly [23].

D. Data processing

For every measurement presented in this work, the raw data frequency ranged from 0.5 to $18\,\mathrm{GHz}$ with increments of $4\,\mathrm{MHz}$. For the probe calibration and tests liquids, the permittivity was computed using the full raw data range. Afterwards, in order to accelerate the permittivity computation for the studied samples (wet and dry paper, wet and dry sand, and soil), the raw data was truncated so that the frequency increments were of $100\,\mathrm{MHz}$ over the range of 0.5 to $18\,\mathrm{GHz}$. This reduced the dataset size, making the computation faster while keeping a sufficient amount of data points to represent the possible variation in the permittivity. Once the permittivity computed, the results were smoothed using the rolling window average or the exponentially weighted moving average methods with a window size of $8.3333\,\%$ of the total range to improve the consistency between measurements.

Since our probe covers a wide frequency range (from 0.5 to $18\,\mathrm{GHz}$), the analysis was made on specific frequencies used in SWE remote sensing. Moreover, in the context of the new satellite mission concept for SWE monitoring (TSMM), the targeted frequencies were also added to the list (Table I).

TABLE I
FREQUENCY BANDS ($\pm 0.25\,\mathrm{GHz}$) ON WHICH THE AVERAGE PERMITTIVITY WAS COMPUTED WITH EXAMPLES OF RELEVANT SATELLITE-BASED SENSORS

Band	Frequency	Satellite example	Ref.
L-band	$1.5\,\mathrm{GHz}$	SMOS ($1.4\,\mathrm{GHz}$)	[25]
C-band	$6.9\,\mathrm{GHz}$	RadarSAT ($5.4\,\mathrm{GHz}$)	[26]
X-band	$10.65\,\mathrm{GHz}$	TerraSAR-X ($9.65\,\mathrm{GHz}$)	[27]
Ku-band 1	$13.5\,\mathrm{GHz}$	TSMM ($13.5\,\mathrm{GHz}$)	[9], [10]
Ku-band 2	$17.2\,\mathrm{GHz}$	TSMM ($17.2\,\mathrm{GHz}$)	

E. Probe signal penetration depth

In order to estimate the probe penetration depth, a test using stacked paper sheet was done [28]. The procedure consisted in progressively stacking sheets of paper on top of a conductive metal plate (copper, high reflectivity). Every few sheets of paper, a permittivity measurement of the paper stack (low relative permittivity) was made. Once the measured permittivity remained constant for additional sheets of paper, it was assumed that the signal contribution from the conductive plate was completely lost, hence the penetration depth of the probe signal was estimated. This test was repeated for dry and wet paper on $216 \times 279\,\mathrm{mm}$ ($8.5 \times 11\,\mathrm{in}$) US letter size printer paper of $0.1\,\mathrm{mm}$ thickness.

F. Soil sample characterization

The probe was used to characterize dry and wet commercial sand and arctic organic mesic soil from Cambridge Bay, Nunavut, Canada ($69.2275°$, $-104.8937°$). The arctic soil sample was collected using a cylindrical PVC soil sample holder of $5\,\mathrm{cm}$ radius and $10\,\mathrm{cm}$ height driven in the soil and excavated so the soil remained undisturbed. The wet sand and organic soil samples were exposed to a temperature ramp from -20 to $20\,^{\circ}\mathrm{C}$ over 10 hours inside a Climats EX-CAL 1411-HE climatic chamber at Laboratoire de l'Intégration du Matériau au Système (IMS, Bordeaux, France). The wet sand and wet organic soil samples were placed in the convection centre of the climatic chamber (Figure 1B). A plastic wrap was used to seal the soil sample cylinder to ensure a constant soil moisture throughout all the temperature cycle. To monitor the soil moisture and soil temperature during the tests, a thermocouple connected to the test chamber was used, as well as a Teros 12 (operating frequency of $70\,\mathrm{MHz}$) soil moisture and temperature probe (METER Group, Inc. USA). The test chamber thermocouple has an approximate length $4\,\mathrm{cm}$ and was inserted in the top layer of the soil sample.

III. RESULTS AND DISCUSSION

A. Probe calibration and test liquids

The calibration curves with the test saline solution ($20\,\mathrm{ppt}$) and methyl hydrate show good agreement with the theoretical values [23] (Figure 2) with Root Mean Squared Error (RMSE) of 1.14 and 0.94 respectively. Figure 2 also highlights the chosen frequency ranges for remote sensing application.

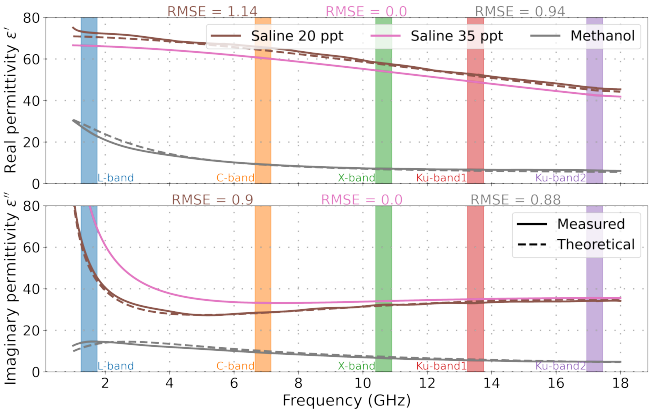

Fig. 2. Theoretical and measured permittivity of saline solution and methanol with their associated RMSE. The selected relevant frequency ranges for remote sensing applications were also highlighted

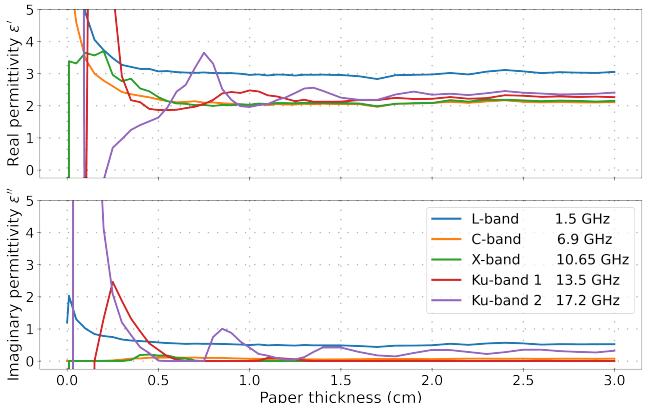

Fig. 3. Estimation of the probe signal penetration depth on dried paper for different relevant frequencies

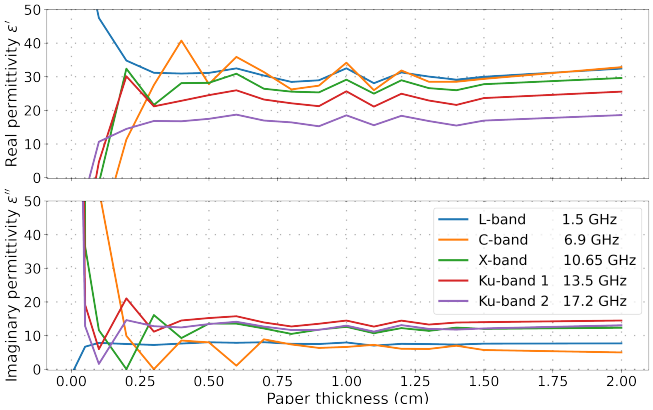

Fig. 4. Estimation of the probe signal penetration depth on soaked paper for different relevant frequencies

B. Signal penetration depth

For dry paper, at L-band (1.4 GHz), the curve was found to stabilize around 0.5 cm for a value $\varepsilon' = 3$ which is coherent with [28] who found a value around $\varepsilon' \approx 2.9$ at 1 GHz. Figure 3 also shows that the probe signal stabilizes around 0.75 cm for the other bands. Knowing that the outer diameter of the probe is of 13.2 mm, these results are consistent with the rule of thumb proposed by El-rayes and Ulaby [28] that the probe penetration depth in a low loss material such as paper is approximately equal to the inside diameter of the outer conducting cylinder of the probe (see left side of figure 1, measurement 2b = 13.2 mm).

Figure 4 results for wetted paper are interpreted similarly. However, since the paper water content increases the dielectric loss, the real permittivity decreases for higher frequencies. It is also noticeable that the loss of signal from the conducting copper plate happens with fewer stacked sheets than with dry paper. The probe's penetration depth in higher loss material can be estimated at around 0.3 cm. Another noticeable difference between the dry and wet paper comes from the oscillations present for both Ku-band frequencies between 0.5 to 1.5 cm for dry paper. These oscillations are the result of noise from unwanted reflection in the dry paper medium. Indeed, the probe signal in a medium such as dry paper at high frequencies, where the wavelengths are closer in scale to the OECP cross-section, is more likely to be reflected on the sample edge and cause unwanted fluctuation in the reflection readings. At frequencies closer to L-band and C-band, where the wavelengths are larger, such unwanted reflections are negligible. In liquids such as the saline solutions used in the probe calibration process or in moist medium such as wet paper, the probe signal is damped, preventing unwanted reflections. Moreover, this signal damping is what causes the penetration depth to be equal across all frequencies in the wet medium. These penetration depths mean that, to safely measure only the desired sample and not its container, a safe minimal soil depth would be over 2 cm. In the present study, the soil sample used are well over this limit with a 10 cm depth.

C. Dry sand spectrum

Since the dry sand permittivity does not vary in this range of temperature, its real and imaginary permittivity are compared to literature data from Matzler [17] (see Figure 5). In [17], the permittivity of dry sand gathered in the Sahara desert in the frequency range of 0.245 to 6 GHz was found to be around $\varepsilon = 2.6 - [0.13, 0.012]\, j$.

Figure 5 shows that the result obtained from the probe used in the present study are consistent with what was found in the literature with a real permittivity slightly above $\varepsilon' = 2$ at lower frequencies and around $\varepsilon' = 2.6$ at the higher end. However, the permittivity measured in this case is below the one from Matzler [17] in their study range of 0.245 to 6 GHz. This can be explained by the grain size or physical properties of the sand [29]. Indeed, varying the density would change the permittivity, where a denser sample would have a higher permittivity since less air ($\varepsilon' = 1$) is present in the analyzed volume.

D. Freezing cycle on wet sand and organic soil

Figure 6 shows results of the temperature cycle on the 25 % weight/weight relative humidity sand. The graph shows that above 0 °C, the permittivity decreases with increasing

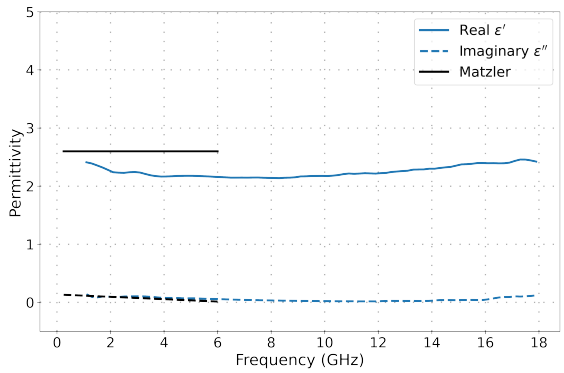

Fig. 5. Measurement of dry sand permittivity on all available frequencies compared to the measurements from Matzler [17]

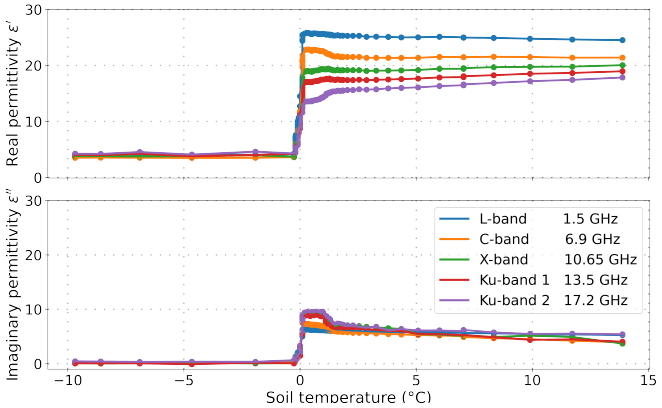

Fig. 6. Freeze/thaw cycle of sand with 25% w/w relative humidity

frequency due to the sand water content, matching what was previously observed for the wet paper (Figure 4) There also seems to be a slight temperature dependency for the Ku-1- and Ku-2- bands where the permittivity increases as temperature rises. This increase is due to the variation of the water permittivity as a function of temperature [30]. At temperatures lower than $0\,^{\circ}\mathrm{C}$, a sharp decrease in permittivity followed by a plateau is observed where all frequencies are approximately at the same value (around $\varepsilon' = 5$).

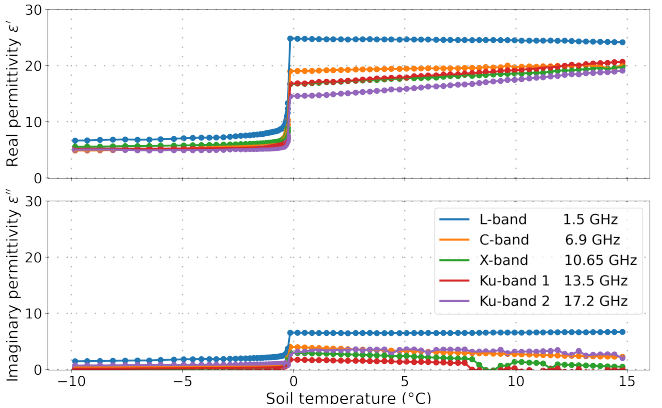

Fig. 7. Freeze/thaw cycle of wet organic mesic soil

Figure 7 shows the permittivity for an Arctic organic soil sample (Cambridge Bay). This sample also seems to show a temperature dependency above $0\,^{\circ}\mathrm{C}$ for the X- and both Ku-bands than the commercial sand where the permittivity increases with the temperature. At $15\,^{\circ}\mathrm{C}$, the permittivity of the organic soil sample for the multiple highlighted frequencies converges around $\varepsilon' = 20$, while the sand sample permittivity is more spread at the same temperature. The below $0\,^{\circ}\mathrm{C}$ permittivity also have sharp drop followed by a plateau when the water inside the sample is completely frozen at a value around $\varepsilon' = 5$, like the commercial sand.

Table II show the average real permittivity of each plateau when the sample is either completely frozen or completely thawed. The uncertainty on the numbers presented in the table comes from a standard deviation from the average. The presented values can be used to parametrize radiative transfer models in order to compute brightness temperature or backscattering coefficients for remote sensing applications.

TABLE II
MEAN REAL PERMITTIVITY OF THE FROZEN ($\mathrm{T} \leq -0.5\,^{\circ}\mathrm{C}$) AND THAWED ($\mathrm{T} \geq 0.5\,^{\circ}\mathrm{C}$) SAMPLE FOR EACH RELEVANT BAND FREQUENCIES

	Wet sand		Organic soil	
	Frozen	Thawed	Frozen	Thawed
L-band (1.5 GHz)	4.03 ± 0.04	25.3 ± 0.2	7.6 ± 0.6	24 ± 2
C-band (6.9 GHz)	3.52 ± 0.02	21.7 ± 0.3	5.8 ± 0.5	19 ± 2
X-band (10.65 GHz)	3.85 ± 0.09	19.2 ± 0.2	6.1 ± 0.3	17 ± 2
Ku-band 1 (13.5 GHz)	4.1 ± 0.2	17.5 ± 0.2	5.4 ± 0.2	17 ± 2
Ku-band 2 (17.2 GHz)	4.3 ± 0.2	15.5 ± 0.5	5.1 ± 0.2	15 ± 2

E. Potential applications for satellite missions

Our unique Open-Ended Coaxial Probe has a large aperture which allows repeatable and precise permittivity measurements of heterogeneous materials while having a frequency band ranging from 0.5 to 18 GHz. Moreover, the permittivity measurements of wet commercial sand and Arctic organic soil sample done in this work show an important variation between frozen and unfrozen soil, and between the highlighted frequency bands above $0\,^{\circ}\mathrm{C}$. This has a special importance for TSMM, where the soil effect on snow water equivalent inversion of from Ku-band SAR is still misunderstood [2], [3]. Furthermore, at Ku-band, possible variability of the frozen soil permittivity due to the soil texture and composition, especially for arctic organic soil, is undetermined. There are also studies showing the effect of the zero-curtain [31], [32] in arctic and boreal forest soil, where the soil under a snowpack is not completely frozen, which can greatly influence the permittivity, hence the backscattering signal.

To follow up this calibration and characterization work with the OECP, we plan on applying the freezing/thawing protocol presented above to an array of soil gathered at different locations to analyze the permittivity as a function of the soil texture, organic matter percentage, temperature and humidity. The database created with these soil characterization will then be used to produce a wideband permittivity model spanning the whole probe range.

IV. Conclusion

In this paper, we present a novel Open-Ended Coaxial Probe that has the ability to measure the permittivity of a heterogeneous sample over a large frequency band (0.5 to $18\,\mathrm{GHz}$), which is of particular interest for the field of microwave remote sensing. In this regard, relevant satellite-based remote sensing sensor frequencies that are commonly used for snow monitoring were chosen in order to present the results. The calibration of the probe shows that it is reliable over all the 0.5 to $18\,\mathrm{GHz}$ range with minimal error (RMSE ≈ 1). Tests on dry and wet stacked paper are used to determine that the penetration depth of the probe signal is between 0.5 to $0.75\,\mathrm{cm}$ depending on the frequency for the dry paper and around $0.3\,\mathrm{cm}$ for wet paper. The probe was also used to measure the permittivity spectrum of dry sand (commercial) and the values were compared to other studies found in the literature. Wet sand (commercial) and wet organic mesic soil sample (Cambridge Bay, Nunavut, Canada) samples were subjected to a temperature ramp varying from -20 to $20\,^{\circ}\mathrm{C}$. Both samples show comparable permittivity/temperature curves where the frozen permittivity is close to $\varepsilon' = 5$ and thawed permittivity revolves around $\varepsilon' = 20$.

Further work using the probe is underway. The OECP permittivity measurements will be used to develop a large band soil permittivity model using the soil composition, humidity and temperature as input. Such a model can be used alongside radiative transfer models such as Snow Microwave Radiative Transfer to compute the emission or backscattering contribution of different surfaces in Snow Water Equivalent retrieval algorithm. This permittivity model will also be tested on real world data coming from the CryoSAR project. A better understanding of the soil contribution to the total backscattering signal at Ku-band frequencies will enable to better understand the relationship between snow microstructure, snow height and snow density in the SWE inversion models that will be used in the Terrestrial Snow Mass Mission.

V. Acknowledgement

The authors would like to thank the Canadian Spatial Agency and Environment and Climate Change Canada teams for their help, Natural Sciences and Engineering Research Council of Canada, Mitacs Globalink and the Bureau des Relations Internationales for funding.

References

[1] J. Shi, C. Xiong, and L. Jiang, "Review of snow water equivalent microwave remote sensing," *Science China Earth Sciences*, vol. 59, no. 4, pp. 731–745, 2016.

[2] J. King, C. Derksen, P. Toose, *et al.*, "The influence of snow microstructure on dual-frequency radar measurements in a tundra environment," *Remote Sensing of Environment*, vol. 215, pp. 242–254, 2018.

[3] N. Rutter, M. J. Sandells, C. Derksen, *et al.*, "Effect of snow microstructure variability on Ku-band radar snow water equivalent retrievals," *The Cryosphere*, vol. 13, no. 11, pp. 3045–3059, 2019.

[4] T. Zhang, "Influence of the seasonal snow cover on the ground thermal regime: An overview," en, *Reviews of Geophysics*, vol. 43, no. 4, 2005.

[5] O. Aygün, C. Kinnard, and S. Campeau, "Impacts of climate change on the hydrology of northern midlatitude cold regions," en, *Progress in Physical Geography: Earth and Environment*, vol. 44, no. 3, pp. 338–375, 2020.

[6] J. Cohen and D. Entekhabi, "The influence of snow cover on northern hemisphere climate variability," *Atmosphere-Ocean*, vol. 39, no. 1, pp. 35–53, 2001.

[7] J. E. Box, W. T. Colgan, T. R. Christensen, *et al.*, "Key indicators of Arctic climate change: 1971–2017," en, *Environmental Research Letters*, vol. 14, no. 4, p. 045 010, 2019.

[8] P. Grogan and S. Jonasson, "Ecosystem CO2 production during winter in a Swedish subarctic region: The relative importance of climate and vegetation type," en, *Global Change Biology*, vol. 12, no. 8, pp. 1479–1495, 2006.

[9] C. Derksen, J. Lemmetyinen, J. King, *et al.*, "A dual-frequency ku-band radar mission concept for seasonal snow," Tech. Rep. providing, 2019.

[10] C. Garnaud, S. Bélair, M. L. Carrera, *et al.*, "Quantifying snow mass mission concept trade-offs using an observing system simulation experiment," *Journal of Hydrometeorology*, vol. 20, no. 1, pp. 155–173, 2019.

[11] Y.-L. S. Tsai, A. Dietz, N. Oppelt, and C. Kuenzer, "Remote Sensing of Snow Cover Using Spaceborne SAR: A Review," en, *Remote Sensing*, vol. 11, no. 12, p. 1456, 2019.

[12] G. Picard, M. Sandells, and H. Löwe, "SMRT: An active–passive microwave radiative transfer model for snow with multiple microstructure and scattering formulations (v1.0)," English, *Geoscientific Model Development*, vol. 11, no. 7, pp. 2763–2788, 2018.

[13] N. Longepe, S. Allain, L. Ferro-Famil, E. Pottier, and Y. Durand, "Snowpack Characterization in Mountainous Regions Using C-Band SAR Data and a Meteorological Model," *IEEE Transactions on Geoscience and Remote Sensing*, vol. 47, no. 2, pp. 406–418, 2009.

[14] M. T. Hallikainen, F. T. Ulaby, M. C. Dobson, M. A. Elrayes, and L.-k. Wu, "Microwave Dielectric Behavior of Wet Soil-Part 1: Empirical Models and Experimental Observations," *IEEE Transactions on Geoscience and Remote Sensing*, vol. GE-23, no. 1, pp. 25–34, 1985.

[15] Y. H. Kerr, P. Waldteufel, P. Richaume, *et al.*, "The SMOS Soil Moisture Retrieval Algorithm," *IEEE Transactions on Geoscience and Remote Sensing*, vol. 50, no. 5, pp. 1384–1403, 2012.

[16] G. C. Topp, J. L. Davis, and A. P. Annan, "Electromagnetic determination of soil water content: Measurements in coaxial transmission lines," en, *Water Resources Research*, vol. 16, no. 3, pp. 574–582, 1980.

[17] C. Matzler, "Microwave permittivity of dry sand," *IEEE Transactions on Geoscience and Remote Sensing*, vol. 36, no. 1, pp. 317–319, 1998.

[18] C. Matzler and U. Wegmuller, "Dielectric properties of freshwater ice at microwave frequencies," en, *Journal of Physics D: Applied Physics*, vol. 20, no. 12, p. 1623, 1987.

[19] M. C. Dobson, F. T. Ulaby, M. T. Hallikainen, and M. A. El-rayes, "Microwave Dielectric Behavior of Wet Soil-Part II: Dielectric Mixing Models," *IEEE Transactions on Geoscience and Remote Sensing*, vol. GE-23, no. 1, pp. 35–46, 1985.

[20] V. L. Mironov, L. G. Kosolapova, and S. V. Fomin, "Physically and mineralogically based spectroscopic dielectric model for moist soils," *IEEE Transactions on Geoscience and Remote Sensing*, vol. 47, no. 7, pp. 2059–2070, 2009.

[21] L. Zhang, T. Zhao, L. Jiang, and S. Zhao, "Estimate of Phase Transition Water Content in Freeze–Thaw Process Using Microwave Radiometer," *IEEE Transactions on Geoscience and Remote Sensing*, vol. 48, no. 12, pp. 4248–4255, 2010.

[22] B. Filali, F. Boone, J. Rhazi, and G. Ballivy, "Design and Calibration of a Large Open-Ended Coaxial Probe for the Measurement of the Dielectric Properties of Concrete," *IEEE Transactions on Microwave Theory and Techniques*, vol. 56, no. 10, pp. 2322–2328, 2008.

[23] A. Nyshadham, C. L. Sibbald, and S. S. Stuchly, "Permittivity measurements using open-ended sensors and reference liquid calibration-an uncertainty analysis," *IEEE Transactions on Microwave Theory and Techniques*, vol. 40, no. 2, pp. 305–314, 1992.

[24] J. Galejs, *Antennas in Inhomogeneous Media*. Elsevier Science & Technology, 1969, p. 294.

[25] Y. H. Kerr, P. Waldteufel, J.-P. Wigneron, *et al.*, "The SMOS Mission: New Tool for Monitoring Key Elements ofthe Global Water Cycle," *Proceedings of the IEEE*, vol. 98, no. 5, pp. 666–687, 2010.

[26] L. C. Morena, K. V. James, and J. Beck, "An introduction to the RADARSAT-2 mission," *Canadian Journal of Remote Sensing*, vol. 30, no. 3, pp. 221–234, 2004.

[27] R. Werninghaus and S. Buckreuss, "The TerraSAR-X Mission and System Design," *IEEE Transactions on Geoscience and Remote Sensing*, vol. 48, no. 2, pp. 606–614, 2010.

[28] M. A. El-rayes and F. T. Ulaby, "Microwave Dielectric Spectrum of Vegetation-Part I: Experimental Observations," *IEEE Transactions on Geoscience and Remote Sensing*, vol. GE-25, no. 5, pp. 541–549, 1987.

[29] T. J. Schmugge, "Effect of Texture on Microwave Emission from Soils," *IEEE Transactions on Geoscience and Remote Sensing*, vol. GE-18, no. 4, pp. 353–361, 1980.

[30] U. Kaatze, "Complex permittivity of water as a function of frequency and temperature," EN, *Journal of Chemical and Engineering Data*, vol. 34, no. 4, pp. 371–374, 1, 1989.

[31] S. I. Outcalt, F. E. Nelson, and K. M. Hinkel, "The zero-curtain effect: Heat and mass transfer across an isothermal region in freezing soil," en, *Water Resources Research*, vol. 26, no. 7, pp. 1509–1516, 1990.

[32] F. Domine, M. Belke-Brea, D. Sarrazin, L. Arnaud, M. Barrere, and M. Poirier, "Soil moisture, wind speed and depth hoar formation in the Arctic snowpack," en, *Journal of Glaciology*, vol. 64, no. 248, pp. 990–1002, 2018.